



Metallic Magnetic Calorimeters for High-Accuracy Nuclear Decay Data

S. T. P. Boyd¹ · G.-B. Kim² · J. A. Hall³ · R. H. Cantor³ · S. Friedrich²

Received: 20 August 2019 / Accepted: 8 February 2020 / Published online: 24 February 2020
© Springer Science+Business Media, LLC, part of Springer Nature 2020

Abstract

Metallic magnetic calorimeters (MMCs) combine the excellent energy resolution of cryogenic gamma ray detectors with a very small nonlinearity and a reproducible response, owing to their magnetization-based sensor and their metallic heat flow path. These attributes make MMCs well suited for photon and particle spectroscopy applications requiring the highest accuracy. We are developing high-resolution MMC gamma ray detectors with the goal of improving the quality of key nuclear decay data for nuclear safeguards and fundamental science. Our exploratory “integrated” (SQUIDs and sensors on the same chip) 14-pixel MMC designs recently demonstrated energy resolution of 37.5 eV at 60 keV. Here, we describe the design and optimization for a new generation of MMC detectors using both “integrated” and “split” designs (SQUIDs and sensors on separate chips). The new designs are expected to have an energy resolution <25 eV (<5 eV) for MMCs optimized for energies up to 100 keV (10 keV) and have up to 32 pixels.

Keywords Nuclear safeguards · Metallic magnetic calorimeter · MMC

1 Introduction

Metallic magnetic calorimeters (MMCs) [1–3] detect particles via the temperature dependence of the sensor magnetization, an equilibrium thermodynamic property. Compared to transition-edge sensors (TES), this simplifies MMC detection physics and reduces sensitivity to microfabrication process conditions. In addition the magnetic sensor, in combination with an all-metallic heat flow path, gives MMC gamma detectors improved linearity and reproducibility compared to TES [4, 5].

✉ S. T. P. Boyd
stpboyd@unm.edu

¹ University of New Mexico, Albuquerque, NM 87131, USA

² Lawrence Livermore National Laboratory, Livermore, CA 94550, USA

³ STAR Cryoelectronics, Santa Fe, NM 87508, USA

These are strong advantages for those spectroscopy applications requiring the highest accuracy.

Our collaboration's exploratory first generation of partially optimized "integrated" (SQUIDs and sensors on the same chip) MMC gamma detectors [5–8] recently demonstrated 37.5 eV FWHM at 60 keV [6, 9]. In this report, we describe the design and initial SQUID test results for a new generation of fully optimized MMC gamma detectors.

2 Mitigating SQUID Power Dissipation in Integrated MMCs

Although our previous MMC detectors performed well [6], pulse heights were reduced due to heating of the paramagnet (PM) by the SQUID bias power (Fig. 1 *top left*). We are pursuing two strategies to reduce this problem.

First, if the heating problem of the integrated MMC designs can be controlled, they will always achieve better energy resolution than split designs [6]. To obtain

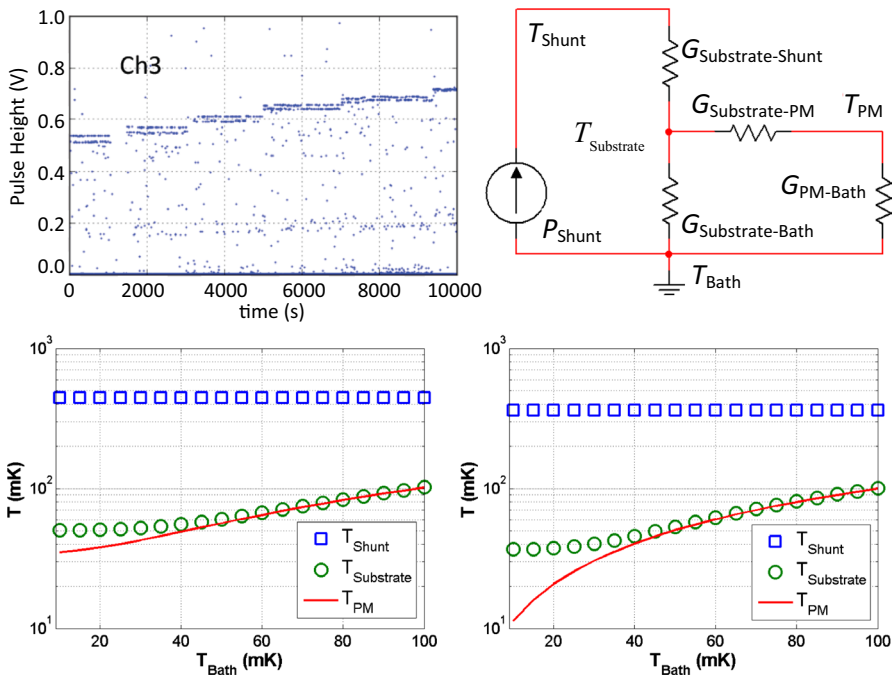


Fig. 1 *Top left* Impact of SQUID bias power heating in the previous generation of integrated MMC detectors: measured positive and negative polarity pulse heights on SQUID channel 3 versus time, increasing in steps as the bias power on SQUID channel 2 is reduced in 6 steps during this time. *Top right* Schematic of a simple thermal model of paramagnet (PM) heating for integrated MMC detectors, see text for explanation. *Bottom left* Model results for the previous generation device, estimating T_{PM} increasingly above T_{Bath} for lower T_{Bath} . *Bottom right* Model results for the new integrated designs, showing T_{PM} closer to T_{Bath} after applying mitigation strategies (color online)

guidance on the heating problem, we can create a simple thermal model (Fig. 1 *top right*). The temperatures in the model are those of the SQUID shunt resistors (T_{Shunt}), the chip ($T_{\text{Substrate}}$), the paramagnet (T_{PM}) and the bath T_{Bath} . Thermal boundary conductances $G_{\text{Substrate-Shunt}}$, $G_{\text{Substrate-PM}}$, and $G_{\text{Substrate-Bath}}$ are modeled using $\dot{Q} = \sigma AT_{\text{hot}}^4 \left[1 - (T_{\text{cold}}/T_{\text{hot}})^4 \right] / 4$, with areas A obtained from the layouts and $\sigma \approx 300 \text{ W m}^{-2} \text{ K}^{-5}$ [10]. The normal-metal thermal conductance $G_{\text{PM-Bath}}$ that sets the pulse decay time is modeled with the Wiedemann–Franz (WF) law $\dot{Q} = \Sigma L_{\text{WF}} T_{\text{hot}}^2 \left[1 - (T_{\text{cold}}/T_{\text{hot}})^2 \right] / 2$, with Σ the electrical conductance and the WF constant $L_{\text{WF}} = 2.44 \times 10^{-8} \text{ W } \Omega \text{ K}^{-2}$. SQUID effective resistance of $1.0 \text{ } \Omega$ at normal operating point is assumed to approximate power dissipation, based on previous electrical measurements with similar SQUID designs. We see immediately that because of the difference in the power-law exponents, for $T_{\text{Substrate}}$ sufficiently low $G_{\text{PM-Bath}}$ will always dominate $G_{\text{Substrate-PM}}$ in determining T_{PM} .

Results from the model corresponding to the previous generation device ($\Sigma = 4.4 \text{ S}$, Josephson junction critical current $I_c = 12 \text{ } \mu\text{A}$, $A_{\text{Substrate-Bath}} = 7.6 \text{ mm}^2$) are shown in Fig. 1 *Bottom Left* for $10 \text{ mK} \leq T_{\text{Bath}} \leq 100 \text{ mK}$. With all 8 SQUIDs biased near $2I_c$, we find $T_{\text{Shunt}} \approx 443 \text{ mK}$, nearly independent of T_{Bath} . $T_{\text{Substrate}}$ deviates from T_{Bath} as T_{Bath} is reduced, settling to $T_{\text{Substrate}} \approx 50 \text{ mK}$ at $T_{\text{Bath}} = 10 \text{ mK}$. $G_{\text{PM-Bath}}$ increasingly dominates $G_{\text{Substrate-PM}}$ at lower T_{Bath} , pulling T_{PM} below $T_{\text{Substrate}}$, but only to $T_{\text{PM}} \approx 35 \text{ mK}$ at $T_{\text{Bath}} = 10 \text{ mK}$.

There are three relatively simple steps we can take to reduce T_{PM} in the new designs. First, $\Sigma_{\text{PM-Bath}}$ increases substantially for $100\text{-}\mu\text{m}$ -thick absorbers with a 1 ms decay constant, to 61 S . Second, we can increase $A_{\text{Substrate-Bath}}$. This can be accomplished by increasing the area of the “front-side thermal bus” [6] on the chip and/or coating normal metal onto the back side of the chip and establishing metallic heat flow between that normal-metal coating and the copper mounting plate at T_{Bath} . Third, we can reduce the SQUID bias power by reducing the I_c below STARCryo’s standard $I_c \cong 12 \text{ } \mu\text{A}$. A recent UNM/STARCryo SQUID array amplifier [11] has demonstrated good performance with I_c as low as $6 \text{ } \mu\text{A}$. In the new MMC wafer, we have reduced I_c to $8 \text{ } \mu\text{A}$ for a $\sim 50\%$ SQUID bias power reduction.

The estimated impact of these changes is shown in Fig. 1 *Bottom Right*. Here $\Sigma = 61 \text{ S}$, $I_c = 8 \text{ } \mu\text{A}$, $A_{\text{Substrate-Bath}} = 12.5 \text{ mm}^2$ (50% coverage). T_{Shunt} is reduced from ~ 443 to $\sim 362 \text{ mK}$, and $T_{\text{Substrate}}$ now reaches $\sim 37 \text{ mK}$ at $T_{\text{Bath}} = 10 \text{ mK}$. This reduction of $T_{\text{Substrate}}$ increases the dominance of $G_{\text{PM-Bath}}$ over $G_{\text{Substrate-PM}}$, allowing T_{PM} to fall to $\sim 11.4 \text{ mK}$ at $T_{\text{Bath}} = 10 \text{ mK}$.

We are currently implementing this strategy with the integrated designs in the new generation of detectors. Effectiveness will be assessed via on-chip PM thermometers included in all designs, with an estimated $\sim 1 \text{ } \mu\text{K}/\sqrt{\text{Hz}}$ near 1 Hz at 20 mK . Note that this cooling strategy requires a fully metallic $G_{\text{PM-Bath}}$. Increased $G_{\text{PM-Bath}}$ for faster pulse decay time or greater maximum energy would further reduce T_{PM} . However, for MMC designs which use $G_{\text{PM-Bath}}$ to connect the PM only to a metallic on-chip thermal reservoir, T_{PM} cannot go below $T_{\text{Substrate}}$ and other mitigation strategies would be required.

Although this approach looks promising for integrated detectors, we have not yet tested it experimentally. For this reason, we are also including devices of the “split”

design in the new generation of detectors (Fig. 2). In split designs, the SQUIDs and sensors are on separate chips, with electrical and mechanical connections arranged to minimize heat transfer. This approach has been thoroughly tested by other groups as their baseline design, but the requirement for wire bonds in the input circuit reduces the performance of flux transformer designs and makes direct-coupled designs impossible.

3 Design and Estimated Performance

The new MMC designs carry forward successful features from the previous generation. All designs make extensive use of the Nb:Ta alloy persistent current switches/shunts with $T_c = 5.3$ K that we developed [8] and demonstrated with MMC [6] for trapping and control of on-chip persistent magnetizing currents. Additionally, a wide Nb:Ta shunt has been added between the bond pads of the magnetizing circuit to improve noise isolation.

All designs maintain the $475 \mu\text{m} \times 475 \mu\text{m}$ size of electroplated gold absorbers. For gamma ray detectors, the absorber thickness is increased to $100 \mu\text{m}$ for $\sim 50\%$ efficiency at 100 keV. Absorbers continue to be fabricated with the dry-film resist process [7]. All designs use “two-layer sensing coils” [6], with a separate magnetizing coil under the sensing coil.

The new designs include sensor coil geometries with and without “superconducting caps” to confine the applied magnetic field to the PM [6]. Comparison between capped and uncapped performance will help quantify the impact of the extra oxide and niobium structures in the capped designs.

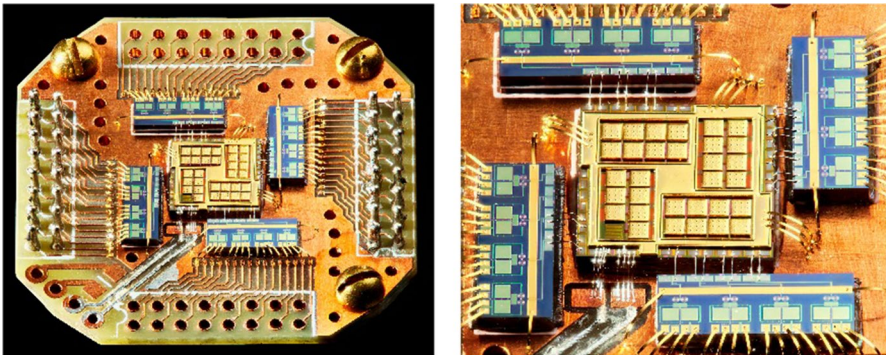


Fig. 2 Two views of the new “split” MMC detector design, in the first fabricated device. Initial tests are under way. 4 “outrigger” chips, each carrying 4 input SQUIDs, surround a central sensor chip with 32 MMC sensors (16 gradiometric pairs). Each sensor except the on-board thermomometer has an electroplated gold absorber $475 \mu\text{m} \times 475 \mu\text{m} \times 100 \mu\text{m}$ thick. Sensors are surrounded by an on-chip electroplated gold “thermal bus.” Input and magnetizing circuit wire bonds are aluminum. SQUID and thermal wire bonds are gold. The solder-tinned traces on the PC board at 7 o’clock connect the magnetizing circuit. The top and bottom connectors are absent due to temporary constraints of the testing setup, and not all of the SQUID input circuits are connected on this first device

The baseline energy resolution [1, 2] ΔE_{FWHM} was optimized for the new designs over 15 two-layer meander sensing coil geometries where trace width and spacing were varied. Natural abundance $\text{Ag}^{\text{nat}}\text{Er}$ PM with a 100 mA magnetizing current was baselined, with Er concentration optimized for each design. The absence of a nuclear electric quadrupole in Ag reduces parasitic heat capacity and yields signals with a single exponential decay constant [5]. Gamma detectors optimized for 100 keV were baselined for a 20 mK dilution refrigerator operating temperature and optimized over PM thicknesses 0.5, 1.0 and 1.5 μm . X-ray detectors optimized for 10 keV were baselined for 30 mK to allow operation in a ^3He -backed ADR and optimized over PM thicknesses 250, 500 and 750 nm.

For the 100 keV integrated gamma detector designs with a transformer coupled series gradiometer topology and an erbium concentration of 300 at. ppm, we estimate ΔE_{FWHM} of 20 eV for a capped and 32 eV for an uncapped PM. With direct coupling, a parallel gradiometer topology with the same PM alloy is expected to improve ΔE to 10 eV capped and 12 eV uncapped.

We estimate that the 10 keV integrated X-ray detector designs with a 1- μm -thick gold absorber, flux transformer coupling and series gradiometer will have ΔE of 3.9 eV capped and 7.6 eV uncapped with an Er concentration of 200 at. ppm. With the same absorber, PM alloy and topology, direct coupling should improve ΔE_{FWHM} to 2.1 eV capped and 2.7 eV uncapped.

Optimization results for the 100 keV split devices (Table 1) show that the presence or absence of the superconducting cap plays a stronger role than the enrichment of the Er. Interestingly, the cap also strongly suppresses the performance variation across the 15 different meander coil geometries.

The estimated baseline resolutions ΔE_{FWHM} for all devices are very sensitive to assumed SQUID white flux noise. A conservative $2 \mu\phi_0/\sqrt{\text{Hz}}$ was baselined, but $1 \mu\phi_0/\sqrt{\text{Hz}}$ has been demonstrated in the UNM cryostat and may be achievable in the dilution refrigerator. At $1 \mu\phi_0/\sqrt{\text{Hz}}$, mean ΔE_{FWHM} for the capped $\text{Ag}^{\text{nat}}\text{Er}$ split design, for example, would drop from 26 to 17 eV.

Table 1 Summary of optimization results for “split” 100 keV MMC gamma ray detectors

	$\text{Ag}^{\text{nat}}\text{Er}$ PM		$\text{Ag}^{\text{168}}\text{Er}$ PM	
	No cap	Cap	No cap	Cap
Mean	35	26	32	24
Std	5.5	1.6	4.6	1.5
Best	28	24	26	22
Worst	46	29	41	27

Numbers are the mean, standard deviation, best and worst values of the optimized baseline FWHM energy resolution ΔE_{FWHM} in eV over the 15 different two-layer meander coil geometries, for each category/column

4 SQUID Design and Test

Optimal MMC energy resolution requires matching the SQUID input inductance to the sensing coils and flux transformer. This matching has the form $L_{\text{input}} = 2L_{\text{sensor}} + L_{\text{parasitic}}$ for a series flux transformer or $L_{\text{input}} = L_{\text{sensor}}/2 + L_{\text{parasitic}}$ for a parallel flux transformer, where L_{sensor} is the inductance of one sensing coil and $L_{\text{parasitic}}$ is the sum of all flux transformer inductance other than the sensing and input coils.

Although series and parallel flux transformers give equal performance for $L_{\text{parasitic}} \ll L_{\text{sensor}}$, the series topology provides better flux transfer into the SQUID when $L_{\text{parasitic}}$ cannot be neglected. Larger flux transfer is equivalent to reducing SQUID noise and thus improves energy resolution. With the two-layer sensing coil, it is equally easy to make the series or parallel topology. The parallel topology was therefore only used for the direct-coupled integrated 100 keV design, in order to reduce the SQUID loop inductance.

To match the new split sensors, a new family of SQUIDs was developed, including our first designs compatible with Magnicon readout electronics [12]. Our previous MMC SQUIDs have been incompatible with Magnicon because they lacked an isolated flux feedback coil: STARCryo's fully differential electronics [13] allows feedback to be applied through one or both SQUID washers, yielding simplified layouts. Magnicon-compatible readout will increase bandwidth, reduce noise, and should also facilitate comparison of results and interoperability of our detectors with other MMC groups.

Dip testing both types of SQUID designs at 4.2 K shows smooth V - ϕ characteristics, a white noise of $\sim 3.5 \mu\phi_0/\sqrt{\text{Hz}}$ (comparable to our previous MMC SQUIDs), and $\leq 5\%$ agreement on calculated feedback coupling.

Acknowledgements This work was funded by the U.S. Department of Energy NA-22 under Grant LL16-MagMicro-PD2La. It was performed under the auspices of the U.S. DOE by Lawrence Livermore National Laboratory under Contract DE-AC52-07NA27344. Calculations were performed at the UNM Center for Advanced Research Computing (CARC). We are grateful to the CARC technical staff for their ongoing support.

References

1. S. Kempf, A. Fleischmann, L. Gastaldo, C. Enss, J. Low Temp. Phys. **193**, 365 (2018). <https://doi.org/10.1007/s10909-018-1891-6>
2. A. Fleischmann, L. Gastaldo, S. Kempf, A. Kirsch, A. Pabinger, C. Pies, J.-P. Porst, P. Ranitzsch, S. Schäfer, F.V. Seggern, T. Wolf, C. Enss, G.M. Seidel, AIP Conf. Proc. **1185**, 571 (2009). <https://doi.org/10.1063/1.3292407>
3. A. Fleischmann, C. Enss, G.M. Seidel, Metallic magnetic calorimeters, in *Cryogenic Particle Detection*, ed. by C. Enss (Springer, Berlin, 2005), pp. 151–216
4. C.R. Bates, C. Pies, S. Kempf, D. Hengstler, A. Fleischmann, L. Gastaldo, C. Enss, S. Friedrich, Appl. Phys. Lett. **109**, 023513 (2016). <https://doi.org/10.1063/1.4958699>
5. G.-B. Kim, R. Hummatov, S. Kempf, C. Flynn, R. Cantor, A. Fleischmann, S.T.P. Boyd, C. Enss, S. Friedrich, J. Radioanal. Nucl. Chem. **318**, 803 (2018). <https://doi.org/10.1007/s10967-018-6182-9>

6. S.T.P. Boyd, R. Hummatov, G.-B. Kim, J.A. Hall, R. Cantor, S. Friedrich, J. Low Temp. Phys. **193**, 435 (2018). <https://doi.org/10.1007/s10909-018-2017-x>
7. R. Hummatov, J.A. Hall, G.-B. Kim, S. Friedrich, R. Cantor, S.T.P. Boyd, J. Low Temp. Phys. **193**, 752 (2018). <https://doi.org/10.1007/s10909-018-1946-8>
8. R. Hummatov, L.N. Le, J.A. Hall, S. Friedrich, R.A. Cantor, S.T.P. Boyd, IEEE Trans. Appl. Supercond. **27**, 2200205 (2017). <https://doi.org/10.1007/s10909-018-1946-8>
9. The Heidelberg MMC group announced a resolution of 9 eV at 60 keV with their maXs-30 device at this conference. To the best of our knowledge MMC detectors now hold the world record for energy resolution in gamma spectroscopy (paper in preparation)
10. Yoon et al., IEEE Trans. Appl. Supercond. **29**, 2300206 (2019). <https://doi.org/10.1109/tasc.2019.2908143> *Although that value of σ was obtained specifically for Au: Er PM deposited onto an MMC readout coil, we anticipate it will remain accurate within about a factor of two for the Au: Pd shunt resistors of the SQUID and for a gold coating on the bottom of the integrated MMC chip*
11. T. de Haan, A. Suzuki, S.T.P. Boyd, R.H. Cantor, A. Coerver, M.A. Dobbs, R. Hennings-Yeomans, W.L. Holzapfel, A.T. Lee, G. Noble, J. Low Temp. Phys. This Special Issue LTD18 (2020)
12. Magnicon GmbH, Barkhausenweg 11, 22339 Hamburg, Germany. <http://www.magnicon.com/squid-electronics/>. Accessed 18 Feb 2020
13. STAR Cryoelectronics LLC, 25-A Bisbee Ct., Santa Fe, NM, 87508. <https://starcryo.com/pcsquid/>. Accessed 18 Feb 2020

Publisher's Note Springer Nature remains neutral with regard to jurisdictional claims in published maps and institutional affiliations.